

Iridium valence variation and carrier sign tuning in $(\text{Ca}, \text{Ba})_x\text{La}_{2-x}\text{CuIrO}_6$ double perovskitesB. A. Duell,¹ Jun Li,¹ D. Haskel,² Jungho Kim,² H. Park,^{3,4} P. G. LaBarre,⁵ A. P. Ramirez⁵ and M. A. Subramanian^{1,*}¹Department of Chemistry, Oregon State University, Corvallis, Oregon 97331, USA²Advanced Photon Source, Argonne National Laboratory, Lemont, Illinois 60439, USA³Department of Physics, University of Illinois at Chicago, Chicago, Illinois 60607, USA⁴Materials Science Division, Argonne National Laboratory, Lemont, Illinois 60439, USA⁵Department of Physics, University of California Santa Cruz, Santa Cruz, California 95064, USA

(Received 11 January 2021; revised 14 March 2021; accepted 27 April 2021; published 10 May 2021)

We report the structure and properties of $(\text{Ca}, \text{Ba})_x\text{La}_{2-x}\text{CuIrO}_6$. The rock-salt double perovskite structure goes through a $P\bar{1}$ to $P2_1/n$ phase transition with increasing Ba content but not with Ca content. In both cases, the Ir ion is oxidized from 4+ to 5+ with increasing substitution. Transport and magnetic properties measurements reveal that all compositions are insulating with hysteretic spin-freezing magnetic behavior. Seebeck coefficient measurements reveal a large thermopower change from $+176 \mu\text{V/K}$ in $\text{La}_2\text{CuIrO}_6$ to $-223 \mu\text{V/K}$ with increasing Ba content in $\text{Ba}_x\text{La}_{2-x}\text{CuIrO}_6$. This behavior is modeled well by the Heikes formula for correlated hopping conduction. $(\text{Ca}, \text{Ba})_x\text{La}_{2-x}\text{CuIrO}_6$ provides a model system for investigations of other systems with similar carrier sign tuning, with applications toward semiconductors and thermoelectric materials.

DOI: [10.1103/PhysRevMaterials.5.054604](https://doi.org/10.1103/PhysRevMaterials.5.054604)

I. INTRODUCTION

There has been large interest in perovskite iridium oxides as templates upon which to investigate novel magnetic and electronic properties. Oxides with iridium as the only transition-metal ion, such as BaIrO_3 , Sr_2IrO_4 , and Sr_4IrO_6 , where iridium is in the 4+ oxidation state, show a range of magnetic and electronic properties, from ferromagnetism and metallic behavior to antiferromagnetism and insulating behavior, caused by the role of onsite repulsion, bandwidth, and spin-orbit (SO) coupling which have similar energy scales in these systems [1–5]. There is a strong interest in studying these materials due to the spin-orbit driven $J_{\text{eff}} = 1/2$ state and its collective effects in frustrated settings, such as the Kitaev honeycomb systems (Na_2IrO_3 , Li_2IrO_3 , etc.). A number of Ir^{5+} perovskites have also been studied in which the behavior reflects the nonmagnetic $5d^4$, $J_{\text{eff}} = 3/2$ state [6–9]. Recently, systems have been studied in which the nominal Ir oxidation state has been varied by adjusting the composition to include other cations that accommodate different charge states [10–16]. It is of interest to explore situations where the Ir valence state is continuously varied, with the prospect of achieving hybridization between local and itinerant charge/spin carriers. The $\text{A}_2\text{B}'\text{B}''\text{O}_6$ double perovskite structure is well studied [17] and is an excellent host for such research. In such studies, however, attention must be paid to the influence of disorder, especially for transport properties. At the extreme end of local environment effects are usually Cu-containing oxides due to the propensity for Cu^{2+} toward Jahn-Teller distortions. However, ambient pressure

Cu/Ir-containing perovskites are rare in the literature, with only $\text{La}_2\text{CuIrO}_6$ and SrLaCuIrO_6 known.

The fully rock-salt ordered double perovskite, $\text{La}_2\text{CuIrO}_6$, shows spin-glass-like collective behavior, while maintaining insulating nature across antiferromagnetic- and ferromagnetic-like transitions. Despite the octahedral (B-site) ordering of the Cu and Ir ions, there exists a large degree of structural distortion. A high degree of octahedral tilt and some octahedral distortion exist as a result of Cu and Ir size mismatch that results in the aforementioned properties [13,18–21]. SrLaCuIrO_6 crystallizes into tetragonal $I4/m$ space group, due to the larger Sr^{2+} ion and despite the structural differences with $\text{La}_2\text{CuIrO}_6$, it remains insulating [9].

The interplay of strong onsite correlations, SO coupling, and structural effects within $\text{La}_2\text{CuIrO}_6$ may give rise to interesting magnetic and transport phenomena through offsite substitution. Both Cu and Ir are known to have multiple valence states that can profoundly influence the properties of materials. Moreover, the evolution of the large degree of structural distortion present in $\text{La}_2\text{CuIrO}_6$ can be investigated through A-site ion size adjustments. We seek to investigate these two parameters, Cu/Ir valence state and structural distortion, on the properties of the system through substitution of the larger Ba^{2+} for La^{3+} in $\text{Ba}_x\text{La}_{2-x}\text{CuIrO}_6$ and the similarly sized Ca^{2+} for La^{3+} in $\text{Ca}_x\text{La}_{2-x}\text{CuIrO}_6$.

II. METHODS

A. Synthesis and characterization

The solid solutions, $\text{Ba}_x\text{La}_{2-x}\text{CuIrO}_6$ and $\text{Ca}_x\text{La}_{2-x}\text{CuIrO}_6$, were synthesized by grinding together stoichiometric amounts of BaCO_3 (Cerac, 99.9%) or CaCO_3 (Mallinckrodt, 99.8%), La_2O_3 (Stanford Materials, 99.99%),

*mas.subramanian@oregonstate.edu

CuO, and IrO₂ in an agate mortar and pestle, pelletizing, and heating to 1373 K in air for 12–24 h. The La₂O₃ was kept in an oven at 1123 K and cooled in a desiccator prior to use. The IrO₂ was made by heating IrCl₃ · xH₂O (Alfa-Aesar, 99.9%) under airflow at 973 K for 12 h. For compositions with Ba ≥ 0.8, synthesis in oxygen atmosphere was required at an elevated temperature of 1423 K. Despite numerous different heating profiles and atmospheric conditions, Ba = 0.9 could not be made phase pure.

Phase identification and lattice parameters were determined on a Rigaku Miniflex II x-ray powder diffractometer. Structural refinements were performed using GSAS EXPGUI software [22] on synchrotron x-ray powder diffraction data collected at 11-BM-B at the Advanced Photon Source (APS), Argonne National Laboratory with a wavelength of 0.457874(1) Å. Powders used for x-ray diffraction were diluted by 7:1 amorphous SiO₂:sample to reduce the absorption coefficient of the specimen.

X-ray absorption spectroscopy (XAS) measurements were performed at the APS beamline 4-ID-D across the Cu K and Ir L_{2,3} absorption edges to determine the Cu and Ir valence states. Sample thickness was optimized for optimal absorption contrast in transmission geometry. High energy harmonics in the x-ray beam were suppressed with use of both harmonic rejection mirrors and by detuning of second crystal in Si(111) double crystal monochromator. Eight samples from the solid solutions Ca_xLa_{2-x}CuIrO₆ ($x = 0, 0.2, 0.4, \text{ and } 0.6$) and Ba_xLa_{2-x}CuIrO₆ ($x = 0.2, 0.5, 0.8, \text{ and } 1.0$) were measured. Reference samples included Cu, Cu₂O, CuO, IrO₂, and Ba₂YIrO₆.

Resonant inelastic x-ray scattering (RIXS) measurements were performed using the RIXS spectrometer at the 27-ID beam line of the Advanced Photon Source where the sample, analyzer, and detector were positioned in the Rowland geometry [23,24]. The diamond(111) high-heat-load monochromator reflects x rays from two in-line undulators into a high-resolution monochromator. The two-bounce monochromator of single monolithic Si(844) channel-cut crystal produces an energy bandpass of 14.8 meV at 11.215 keV. The beam is then focused by a set of Kirkpatrick-Baez mirrors, yielding a typical spot size of 10 × 40 μm² (v × h) at the sample. A horizontal scattering geometry was used with the incident photon polarization in the scattering plane. All data were collected with the 90° scattering angle to minimize the contribution from the Thompson elastic scattering. The Si(844) diced spherical analyzer and the position-sensitive silicon microstrip detector produced an overall energy resolution of FWHM = 30 meV.

Low-temperature magnetic measurements were performed with a Quantum Design MPMS equipped with a superconducting quantum interference device (SQUID). Electrical resistivity and Seebeck coefficient measurements were collected on dense polycrystalline bars approximately 0.3 × 0.3 × 1.2 cm in dimension in a ULVAC ZEM-3 instrument under helium atmosphere from 300 to 800 K.

B. Theoretical methods

Density functional theory (DFT)+*U* calculations were performed using Vienna *ab initio* simulation package (VASP)

[25,26]. The Perdew-Burke-Ernzerhof (PBE) implementation was used as the exchange-correlation functional [27]. We used the experimentally determined structure to compute the density of states with and without the spin-orbit (SO) effect. For the Cu ion, we used the Hubbard *U* value as 5 eV and the Hunds coupling *J* as 0.8 eV. For the Ir ion, we set *U* = 2.5 eV and *J* = 0.4 eV. The gamma-centered Monkhorst-Pack *k*-point mesh of 8 × 6 × 8 was adopted for all structures. The energy cutoff for the plane-wave basis was used as 400 eV.

III. RESULTS AND DISCUSSION

A. Structural characterization

Rietveld analysis of high-resolution synchrotron powder x-ray diffraction data for La₂CuIrO₆ converged to the triclinic *P* $\bar{1}$ double perovskite structure reported by Manna *et al.* [18]. A solid solution exists for Ba_xLa_{2-x}CuIrO₆ for 0 ≤ *x* ≤ 0.8 and *x* = 1 (see Supplemental Material [28]). Ba_{0.9}La_{1.1}CuIrO₆ could not be made phase pure and compositions where *x* > 1 had increasing amounts of the hexagonal phase, Ba₅CuIr₃O₁₂. The x-ray diffraction (XRD) patterns can be found in the Supplemental Material. The large size difference in Ba²⁺ and La³⁺ causes the unit cell volume to increase with increasing Ba²⁺ content (Fig. 1) [20]. Between 0 ≤ *x* ≤ 0.5 triclinic symmetry is maintained. Fitting of the XRD data is complicated by the slow convergence of the (200), (1 $\bar{2}$ 1), (1 $\bar{2}$ 1), (002), (1 $\bar{2}$ 1), and (121) peaks between *x* = 0.2 and *x* = 1.0 Ba content. The convergence of these peaks indicates an increase in symmetry from triclinic. This tends to happen in perovskites where the octahedral distortion is eased. The relative distortion can be determined by the formula,

$$t = \left(\frac{r_A + r_O}{2(r_B + r_O)} \right)^{1/2}, \quad (1)$$

where *t* is the tolerance factor, *r_A* is the *A* site radius, *r_B* is the *B* site radius, and *r_O* is the radius of the anion [29]. Perovskites with *t* < 1 generally have monoclinic or orthorhombic symmetry. For La₂CuIrO₆, the tolerance factor is approximately 0.939, suggesting a large degree of octahedral tilt/distortion should occur, which is confirmed by the triclinic symmetry. Substitution of Ba²⁺ increases the tolerance factor significantly, theoretically easing the octahedral tilt. Above *x* = 0.5 Ba content, the unit cell can be modelled as *P*₂₁/*n* with the *a* and *c* lattice parameters steadily approaching an approximate value of 5.72 Å. The BaLaCuIrO₆ end member has an expected tolerance factor of 0.995 if iridium is in the 5+ oxidation state. Despite a tolerance factor of nearly 1, the monoclinic unit cell (Table I) remains the best model after Rietveld analysis, in contrast to SrLaCuIrO₆ which is tetragonal (Fig. 2). The low symmetry of BaLaCuIrO₆ can be attributed to the size difference between Ir⁴⁺ or Ir⁵⁺ and Cu²⁺, which have average *B*-O (*B* = Cu, Ir) bond lengths of 1.978(13) Å and 2.054(13) Å, respectively (Table II). The Cu-O3 bond is also elongated at 2.234(3) Å, which is significantly more pronounced than in La₂CuIrO₆. The smaller size of Ir⁵⁺ compared to Ir⁴⁺ alone cannot explain this octahedral distortion, as it would be expected that all bond lengths would be affected. Jahn-Teller effects are common in Cu²⁺-containing

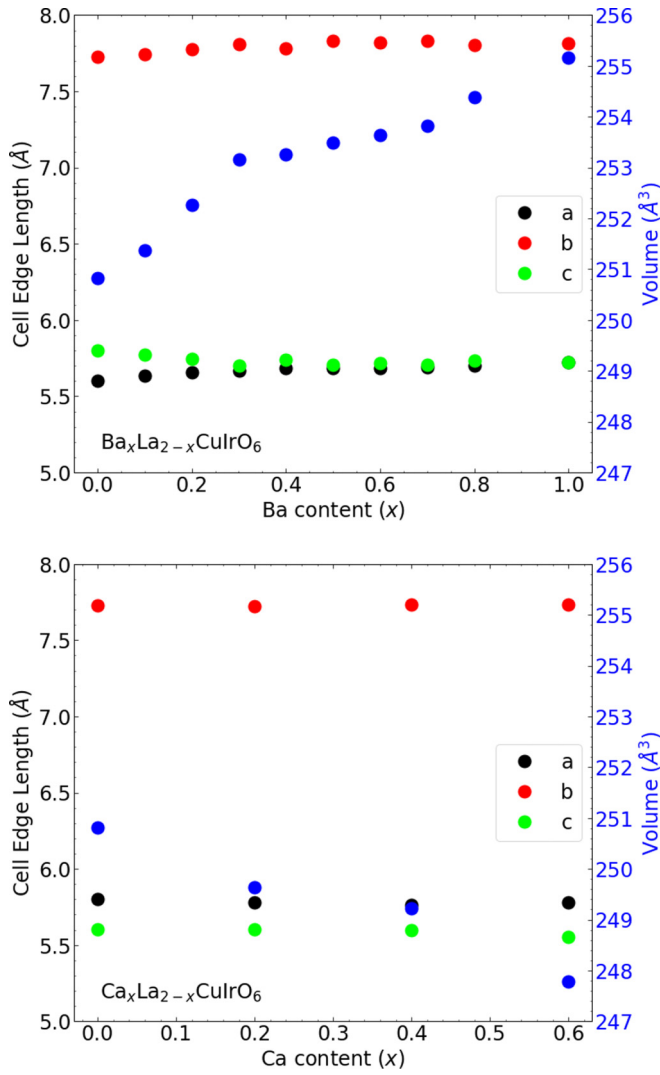


FIG. 1. Unit cell parameters of $\text{Ba}_x\text{La}_{2-x}\text{CuIrO}_6$ (top) and $\text{Ca}_x\text{La}_{2-x}\text{CuIrO}_6$ as a function of Ba/Ca content. The blue circles and right axes show the volume change. The cell edge and volume changes of $\text{Ca}_x\text{La}_{2-x}\text{CuIrO}_6$ are smaller than $\text{Ba}_x\text{La}_{2-x}\text{CuIrO}_6$ due to the similar size of Ca^{2+} and La^{3+} .

oxides and a pronounced Jahn-Teller distortion is observed in SrLaCuIrO_6 [9]. Examination of the unit cell of BaLaCuIrO_6 , shown in Fig. 3, reveals highly distorted CuO_6 octahedra but relatively rigid IrO_6 octahedra. These distortions can be quantified by the bond distortion index,

$$D = \frac{1}{n} \sum_{i=1}^n \frac{l_i - l_{\text{av}}}{l_{\text{av}}}, \quad (2)$$

where n is the number of bonds, l_i is a particular bond length, and l_{av} is the average bond length of the polyhedron, and the quadratic elongation

$$\langle \lambda \rangle = \frac{1}{n} \sum_{i=1}^n \frac{l_i}{l_{\text{av}}} \quad (3)$$

which describes the lengthening or shortening of an axis compared to the average polyhedral length [30,31]. The values of these indices for the Cu and Ir octahedra are shown in

TABLE I. Refined atomic parameters of BaLaCuIrO_6 . Note: Rietveld refinement converged to a monoclinic $\text{P2}_1/\text{n}$ symmetry with $a = 5.72135(2)$ Å, $b = 7.81172(3)$ Å, $c = 5.72291(1)$ Å, and $\beta = 86.033(1)^\circ$ and $\chi^2 = 5.742$ and $\text{Rw} = 9.59\%$.

	x	y	z	Occ.	U_{iso} (Å ²)
Ba	0.5004(5)	0.2513(2)	0.4997(6)	0.5	0.0089(2)
La	0.5004(5)	0.2513(2)	0.4997(6)	0.5	0.0089(2)
Cu	0	0	0	1	0.0016(3)
Ir	0.5	0	0	1	0.0084(1)
O1	0.235(2)	-0.0395(9)	0.245(1)	1	0.024(3)
O2	0.465(2)	0.246(1)	0.021(2)	1	0.015(2)
O3	0.290(1)	-0.002(4)	0.00(6)	1	0.009(1)

Table III. It is clear that there is no significant distortion in the Ir octahedra with Ba substitution, but the Cu octahedra become significantly more distorted. This IrO_6 rigidity is likely due to the high charge density of $\text{Ir}^{4+}/\text{Ir}^{5+}$. The elongation of the apical (Cu-O3) would then be due to a cooperative Jahn-Teller distortion and rigid yet twisted IrO_6 octahedra. Thus, BaLaCuIrO_6 remains a highly twisted monoclinic double perovskite due to the large size differences of the A and B site ions and the loss of suppression of a Jahn-Teller distortion.

A solid solution exists for $\text{Ca}_x\text{La}_{2-x}\text{CuIrO}_6$ where $0 \leq x \leq 0.6$ (see Supplemental Material). Unit cell volume, shown in Fig. 1, decreases slightly with the addition of Ca, consistent with the small size difference between Ca^{2+} and La^{3+} [20]. Contrary to the Ba substitution, the symmetry does not increase with increasing substitution. The reduction in octahedral tilt from Ba substitution does not occur with Ca substitution. Rietveld analysis of $\text{Ca}_{0.2}\text{La}_{1.8}\text{CuIrO}_6$ shows no disorder of Cu and Ir ions, which would cause a reduction in intensity of (110), (1 $\bar{1}$ 0), (011), and (01 $\bar{1}$) peaks. This is consistent with the Ba substitution. As with the Ba substitution, substitution of Ca causes an elongation of one set

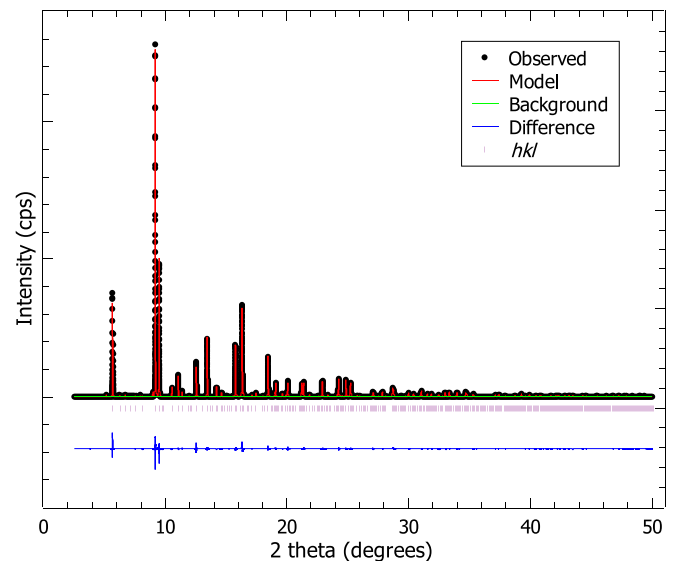


FIG. 2. Rietveld refinement of BaLaCuIrO_6 from high-resolution synchrotron data.

TABLE II. Bond lengths (\AA) and bond valence sums (BVS) of B site ions in BaLaCuIrO₆.

	O1	O2	O3	Ave. bond length	BVS
Cu	1.939(10)	1.991(10)	2.231(10)	2.054(17)	2.30
Ir	2.016(11)	1.941(10)	1.972(3)	1.976(15)	5.11

of Cu-O bonds coupled with smaller Ir octahedra, consistent with an average oxidation state increase of Ir, which we confirm with XAS and RIXS measurements, discussed below. Refinement of site occupancies, shown in Table IV, for Ca and La showed a slight increase in Ca content from the nominal composition. This could be due to the heating conditions wherein La leeches slightly into the alumina crucibles used.

B. XAS and RIXS characterization

XAS measurements across the Cu *K* (Fig. 4) and Ir *L*₂ and *L*₃ (Fig. 5) absorption edges were used to identify the evolution of the Cu and Ir oxidation states with Ba²⁺ and Ca²⁺ substitution. The Cu *K* absorption edge involves primarily a 1*s* to 4*p* electric dipole transition, however, a pre-edge peak resulting from the symmetry forbidden 3*d* transition commonly occurs when the Cu site point group lacks inversion symmetry. The lack of a sizable pre-edge in our data confirms that the Cu sites are centrosymmetric and suggests that there is a lack of strong hybridization between Cu 3*d* and 4*p* bands. For both Ba-substituted and Ca-substituted samples, there is no systematic shift in absorption as a function of composition, indicating the valence of Cu is not changing significantly. The bond valence sum (BVS) [32] between La₂CuIrO₆ and BaLaCuIrO₆ of 1.99 and 2.30 corroborates that the Cu valence does not change significantly. The Ir *L*₂ and *L*₃ absorption edges probe the 5*d* states. A steady shift is observed in both the *L*₂ and *L*₃

TABLE III. Bond distortions (*D*) and quadratic elongations (λ) of the Cu and Ir sites between La₂CuIrO₆ and BaLaCuIrO₆. The Cu sites of BaLaCuIrO₆ are more distorted.

	La ₂ CuIrO ₆	BaLaCuIrO ₆
<i>D</i> -Cu	0.0327(1)	0.0573(1)
<i>D</i> -Ir	0.0176(1)5	0.0135(1)
λ -Cu	1.00(1)	1.03(1)
λ -Ir	1.00(1)	1.00(1)

edges, indicating a larger systematic change in Ir valence than that of the Cu. From this XAS data, the calculated Ir valence (Fig. 6), referenced to the nominal +4.0 in the La₂CuIrO₆ parent compound is $+4.75 \pm 0.05$ at $x = 1$ Ba.

In Fig. 7 we show the RIXS spectra of Ba₂YIrO₆ and BaLaCuIrO₆. Both systems are found to have the same number of excitation peaks. The elastic scattering is seen at the zero energy loss and three sharp inelastic peaks are identified below 2 eV energy loss. At larger energy loss than 2 eV, broad features are seen at around 4, 6, and 9 eV. Previous RIXS measurements on Ba₂YIrO₆ have associated three sharp inelastic peaks below 2 eV to the *t*_{2g} multiplet levels of *d*⁴ configurations including the spin-orbit coupling and the Hund's coupling [33,34]. The broad feature at around 4 eV corresponds to the crystal-field excitation (i.e., excitations between *t*_{2g} and *e*_g levels) and two higher features at around 6 and 9 eV are assigned to charge-transfer excitations. The RIXS spectrum of BaLaCuIrO₆ can be interpreted in the same way and establishes that the Ir ions have *d*⁴ (5+) configuration.

Figure 8 shows RIXS spectra of BaLaCuIrO₆, Ba_{0.5}La_{1.5}CuIrO₆, Ca_{0.5}La_{1.5}CuIrO₆, and La₂CuIrO₆. The difference among those systems is seen in the low energy loss region below 2 eV. As the La content increases, the lowest energy loss peak around 300 meV is weakened while

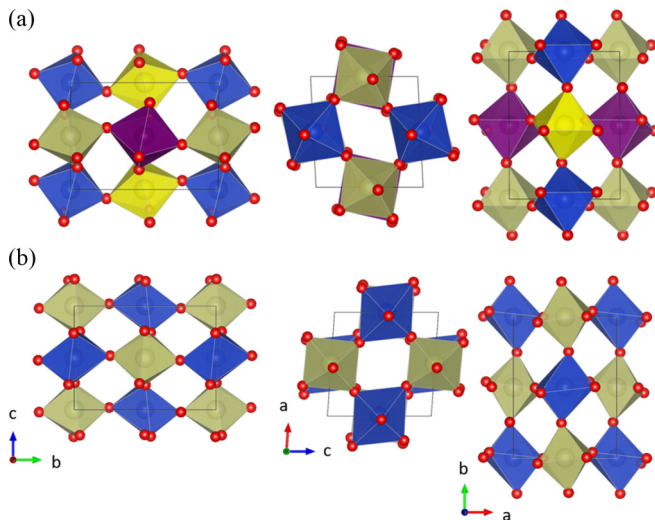


FIG. 3. The unit cell of (a) La₂CuIrO₆ and (b) BaLaCuIrO₆ along each axis is shown. A-site ions (*A* = Ba, La) are not shown for clarity. Cu octahedra are blue and violet and Ir octahedra are tan and yellow.

TABLE IV. Refined atomic parameters of nominal Ca_{0.2}La_{1.8}CuIrO₆. Rietveld refinement converged to a triclinic *P* $\bar{1}$ symmetry with $a = 5.77706(2)$ \AA , $b = 7.72115(1)$ \AA , $c = 5.60454(1)$ \AA , $\alpha = 89.850(1)^\circ$, $\beta = 93.063(1)^\circ$, $\gamma = 90.202(1)^\circ$, and $\chi^2 = 3.028$ and $Rw = 7.55\%$.

	<i>x</i>	<i>y</i>	<i>z</i>	Occ.	<i>U</i> _{iso} (\AA^2)
Ca1	0.5530(1)	0.24933(9)	0.4945(1)	0.133(2)	0.0131(2)
La1	0.5530(1)	0.24933(9)	0.4945(1)	0.867(2)	0.0131(2)
Ca2	-0.0496(2)	0.74981(9)	-0.0110(1)	0.134(2)	0.0129(2)
La2	-0.0496(2)	0.74981(9)	-0.0110(1)	0.866(2)	0.0129(2)
Cu1	0.5	0	0	1	0.007(3)
Cu2	0	0.5	0.5	1	0.008(6)
Ir1	0	0	0.5	1	0.0116(2)
Ir2	0.5	0.5	0	1	0.0119(2)
O1	0.286(1)	0.0426(8)	0.314(1)	1	0.010(2)
O2	0.318(1)	0.4592(8)	0.292(1)	1	0.008(2)
O3	0.2031(8)	-0.0473(6)	0.798(1)	1	0.003(1)
O4	0.200(1)	0.5478(8)	0.821(1)	1	0.018(2)
O5	0.4732(8)	0.2430(8)	0.911(1)	1	0.006(1)
O6	0.0228(8)	0.7464(8)	0.423(1)	1	0.002(1)

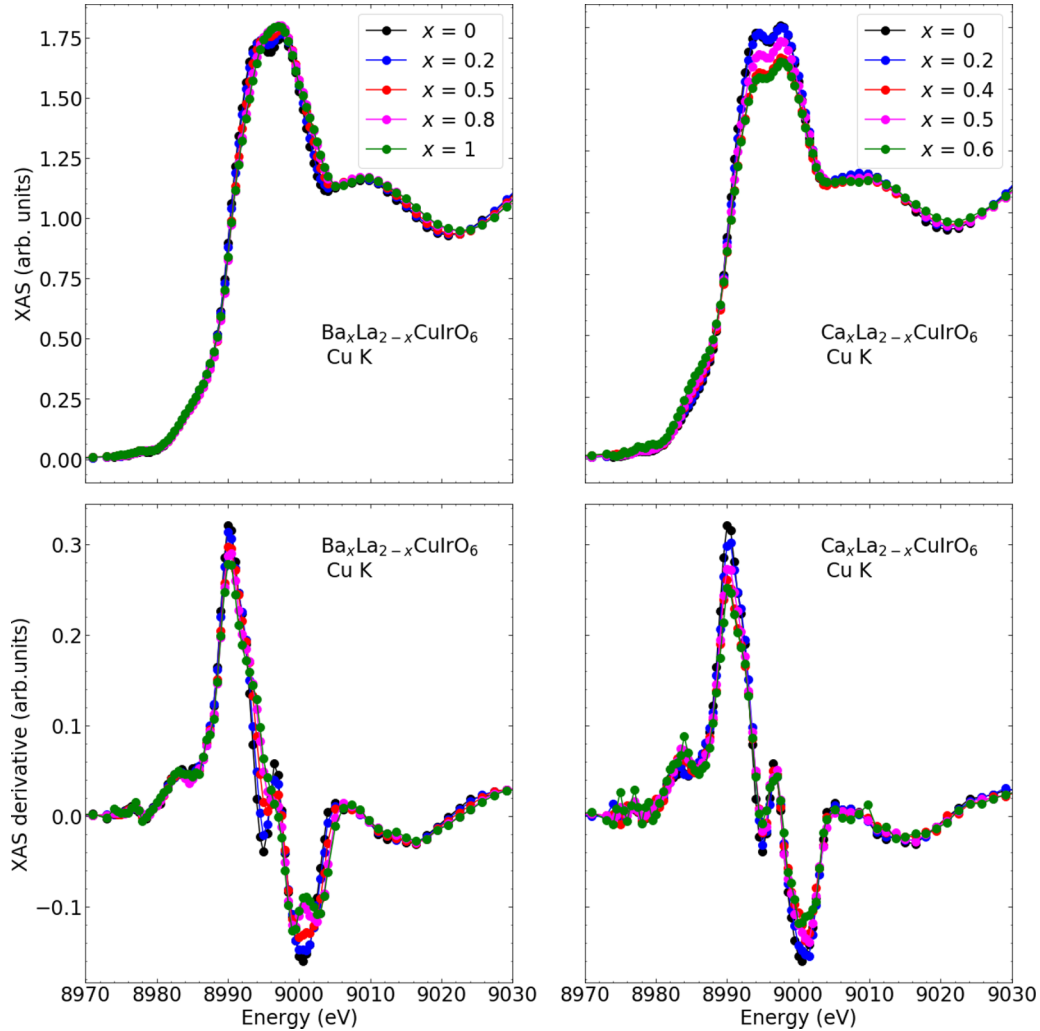


FIG. 4. XAS measurements (top) and derivatives (bottom) of $\text{Ba}_x\text{La}_{2-x}\text{CuIrO}_6$ and $\text{Ca}_x\text{La}_{2-x}\text{CuIrO}_6$ at the Cu K absorption edge. The absence of a systematic shift in absorption shows Cu is not being oxidized with increasing x .

a new peak grows at 720 meV. The RIXS study on $\text{Sr}_3\text{CuIrO}_6$ observed two peaks between 500 and 1000 meV and assigned those peaks to the t_{2g} multiplet levels of d^5 configurations in the noncubic crystal environment [35]. The RIXS spectrum of $\text{La}_2\text{CuIrO}_6$ can be interpreted in the same way and establishes that the Ir ions have d^5 ($4+$) configuration. RIXS spectra of $\text{Ba}_{0.5}\text{La}_{1.5}\text{CuIrO}_6$ and $\text{Ca}_{0.5}\text{La}_{1.5}\text{CuIrO}_6$ show weaker intensities of the 720 meV peak, indicating that the Ir valences in these systems are intermediate between $4+$ and $5+$.

C. Density of states from first principles

In Fig. 9, we display the density of states computed using DFT+ U and DFT+ U +SO for both $\text{La}_2\text{CuIrO}_6$ and BaLaCuIrO_6 . The local Hubbard U values used for Cu $3d$ orbitals and Ir $5d$ orbitals in our calculations are consistent with the previous values used in the literature [36–38] although the screened U values can be changed depending on the energy window chosen to describe the correlated orbitals. The U value used in Ir is smaller than the Cu U value since $5d$ orbitals are spatially more extended and the Hubbard interaction between them is more screened due to the larger

bandwidth than the case of $3d$ orbitals. Similarly to already known oxide material calculations, the role of U and J in this case is important to stabilize the insulating state since our DFT+SO calculations exhibit metallic states in both compounds, although the hole density values are quite similar to the DFT+ U +SO results. The full comparison of the DOS with and without U and SO calculations is shown in the Supplemental Material. Consistent with experimental results, the calculated hole density (integrated density of states in unoccupied states) in the Cu ion does not change much while the hole density in the Ir ion has increased by 0.4 as La is replaced by Ba ($x = 1$). This means that the Ir oxidation number has increased by 0.4 while the Cu oxidation state did not change much, which is similar to the analysis of the XAS and RIXS data. The SO effect strongly affects the low-energy density of states in BaLaCuIrO_6 . The ground state of BaLaCuIrO_6 computed in DFT+ U is metallic while the DFT+ U +SO ground state is insulating showing the importance of the SO effect in opening the spectral gap at the Fermi energy. This is because of the band narrowing of the Ir d states due to the SO effect, hence enhancing the electronic correlation effect. The feature of the unoccupied density of states in DFT+ U +SO exhibits

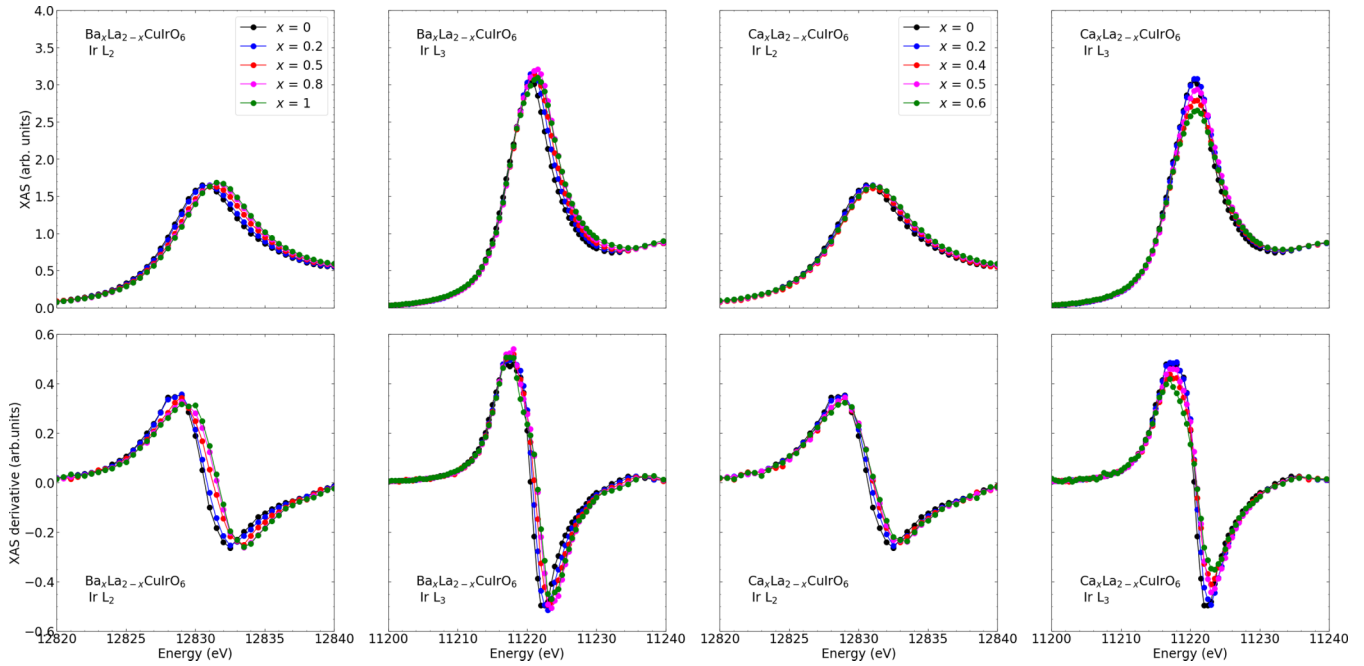


FIG. 5. XAS measurements (top) and derivatives (bottom) of $\text{Ba}_x\text{La}_{2-x}\text{CuIrO}_6$ and $\text{Ca}_x\text{La}_{2-x}\text{CuIrO}_6$ at the Ir L_2 and L_3 absorption edges. A systematic shift in both the L_2 and L_3 absorption edges shows Ir is oxidized with increasing x .

the noticeable peak splitting of the Ir t_{2g} state compared to the DFT+ U case without SO due to the energy splitting between $j_{\text{eff}} = 1/2$ and $j_{\text{eff}} = 3/2$ states which are also strongly mixed in the noncubic crystal environment. These peaks are more pronounced and move to lower energy in BaLaCuIrO_6 as the Ir oxidation number has increased although the peak splitting is slightly reduced.

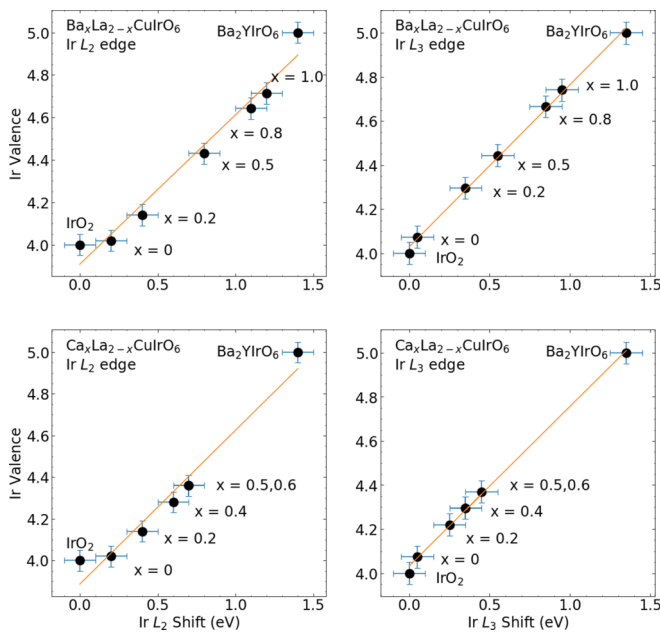


FIG. 6. The calculated Ir valence in $\text{Ba}_x\text{La}_{2-x}\text{CuIrO}_6$ and $\text{Ca}_x\text{La}_{2-x}\text{CuIrO}_6$ at the Ir L_2 and L_3 absorption edges. The solid lines are calculated best fits to the data.

D. Transport properties

All samples are semiconducting across all measured temperatures as shown in Fig. 10. Arrhenius plots of the high temperature resistivity data are not perfectly linear (Fig. 10). The calculated transport gaps between the low and high-temperature regions of the collected data also differ, behavior that is not seen in intrinsic semiconductors, which have a temperature-independent gap energy. The resistivity can be fit over the entire measured temperature range to three-dimensional variable-range charge-hopping (VRH), $\rho = \rho_0 \exp(T_0/T)^{1/4}$, which shows a linear relationship for $\ln \rho$ vs $T^{-1/4}$ (Fig. 10). The calculated T_0 values from this data range from 8×10^7 to 2×10^{13} K, which are exceptionally large and underscore the localization present in both these solid solutions. These large values may arise from the tendency of Ir to localize electrons due to its SO interaction [39]. The VRH model is reinforced by the Seebeck measurements.

In Fig. 11 we show the Seebeck coefficient, S , versus temperature for $\text{Ba}_x\text{La}_{2-x}\text{CuIrO}_6$ and $\text{Ca}_x\text{La}_{2-x}\text{CuIrO}_6$. Except for the samples with low $|S|$ for which S crosses zero, all of the data in the temperature range 300–800 K exhibit $d|S|/dT \leq 0$, which is consistent with the hoppinglike resistivity shown in Fig. 10 for all of these compounds.

Most surprising about the Seebeck data in Fig. 11 is the dependence of the carrier sign on x , coupled with the large magnitude at the opposite polarity end points. We see a clear systematic increase of electronlike transport with increasing x . For $x = 0$, the $S(320 \text{ K}) = 176 \mu\text{V/K}$ whereas for $x = 1$, $S(320 \text{ K}) = -223 \mu\text{V/K}$, with $S = 0$ at $x \approx 0.37$. In order to better understand this behavior, we plot in Fig. 12 $S(x)$ for $T = 320 \text{ K}$ and 725 K , a temperature range that encompasses most of the likely applications of these materials for

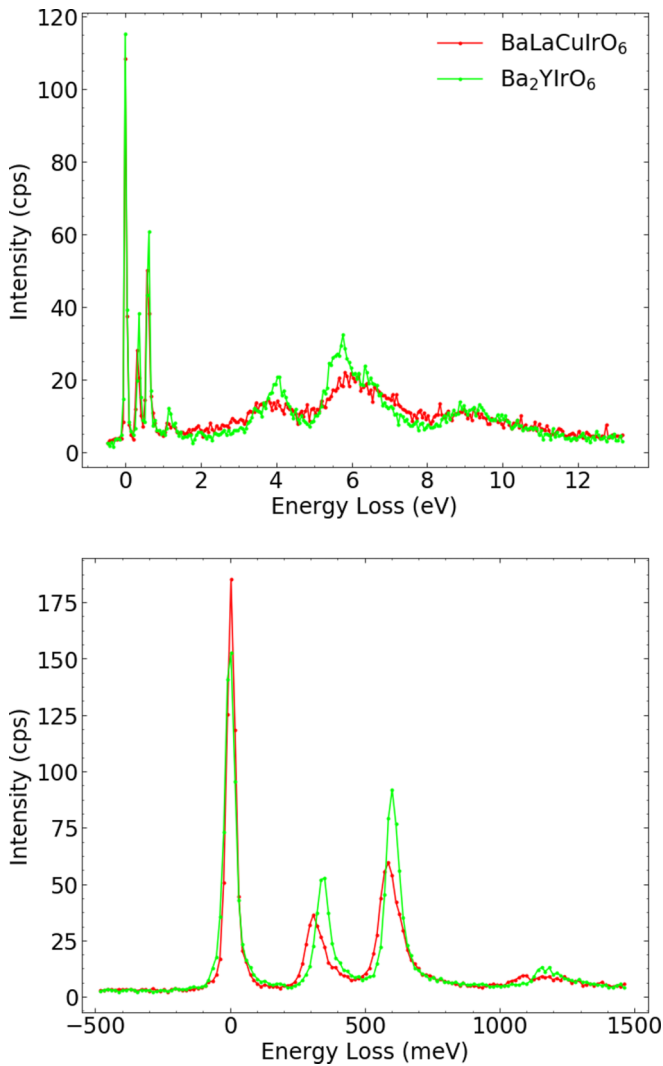


FIG. 7. Comparison of the RIXS data of Ba_2YIrO_6 and BaLaCuIrO_6 . The similar peak configurations of the compounds show Ir in BaLaCuIrO_6 to be in the $5+$ configuration.

thermoelectric power generation or cooling. The clear change in sign around $x = 0.4$, in addition to the large values at the dilution limits of $x = 0$ and $x = 1$, suggests that light band doping scenarios are not at work. Given that $\rho(T)$ is well described by variable-range hopping, as well as the expectation of strong on-site localization due to large SOC, we compare our $S(x)$ data with the Heikes model. This is a statistical model that assumes only single occupancy per hopping site and yields

$$S = (k_B/e) \frac{1 - \zeta}{\zeta} \quad (4)$$

where $\zeta = N_h/N_d$, with N_h being the density of holes and N_d the density of defect-generated hopping sites [40]. This formula, which is the simplest model that describes the observed sign change of S , is plotted in Fig. 12 with no adjustable parameters and also with the charge neutrality shifted to $x = 0.37$ by assuming that $\zeta = x - 0.13$. Such a shift implies that the $x = 0$ end member already has approximately 13% of the hopping sites occupied by electrons, a picture that is

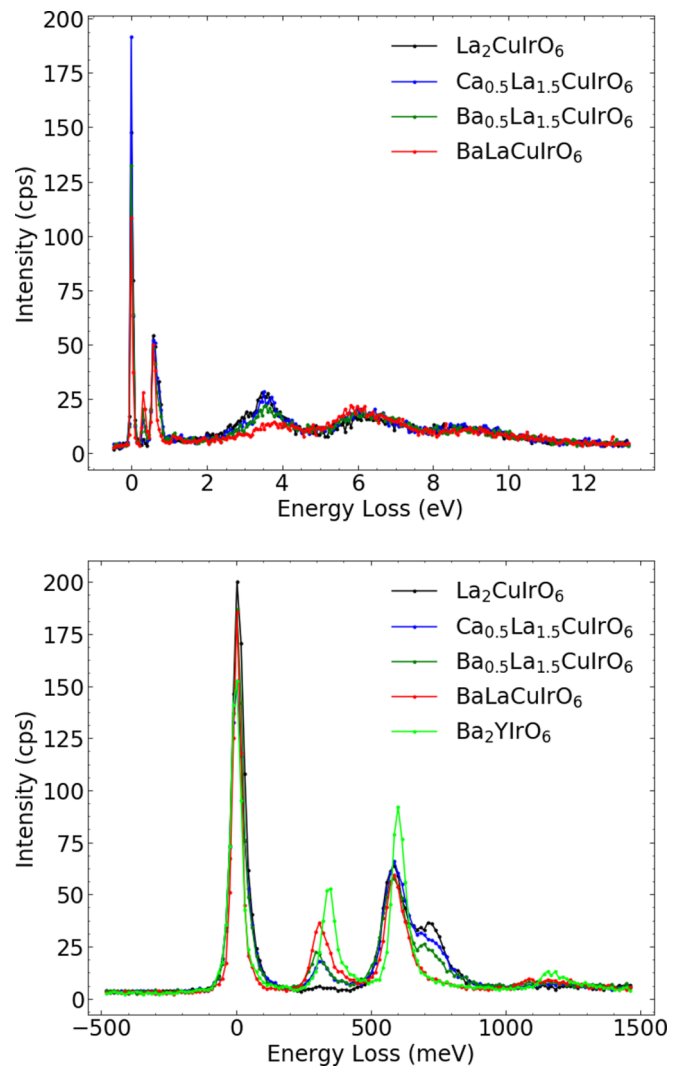


FIG. 8. RIXS data of selected compositions of $(\text{Ca}, \text{Ba})_x\text{La}_{2-x}\text{CuIrO}_6$ with comparison to Ba_2YIrO_6 as an Ir^{5+} reference. The peaks shifting towards higher energy loss with increasing x signals the oxidation of Ir from $4+$ to $5+$.

supported by the fact that $|S|(0) < |S|(1)$. We see that the data are reasonably well described for $x < 0.7$, supporting the basic model of hopping among sites with strong interaction energy in the high temperature regime, $U_0 \lll k_B T$, where U_0 is the onsite Coulomb interaction [40]. The Heikes formula describes the data at $T = 320$ K fairly well, though the data at 725 K display a smaller difference between $S(0)$ and $S(1)$, an affect that may be ascribed to the general behavior of a semiconductor, namely the decrease in energy needed to promote a carrier to the conduction band on increasing temperature. While a sign change in S has been seen in other systems, the agreement with the simple Heikes model is particularly good for $\text{Ba}_x\text{La}_{2-x}\text{CuIrO}_6$. Some cobaltates for example, such as Sr- and Ce-doped LaCoO_3 , show conduction behavior consistent with the Heikes model but also show a sign change consistent with the doping type [41]. In LaMnO_3 , a temperature dependent sign change in the Seebeck coefficient at high temperature occurs due to a Jahn-Teller orbital ordering causing a change from polaron-mediated to charge

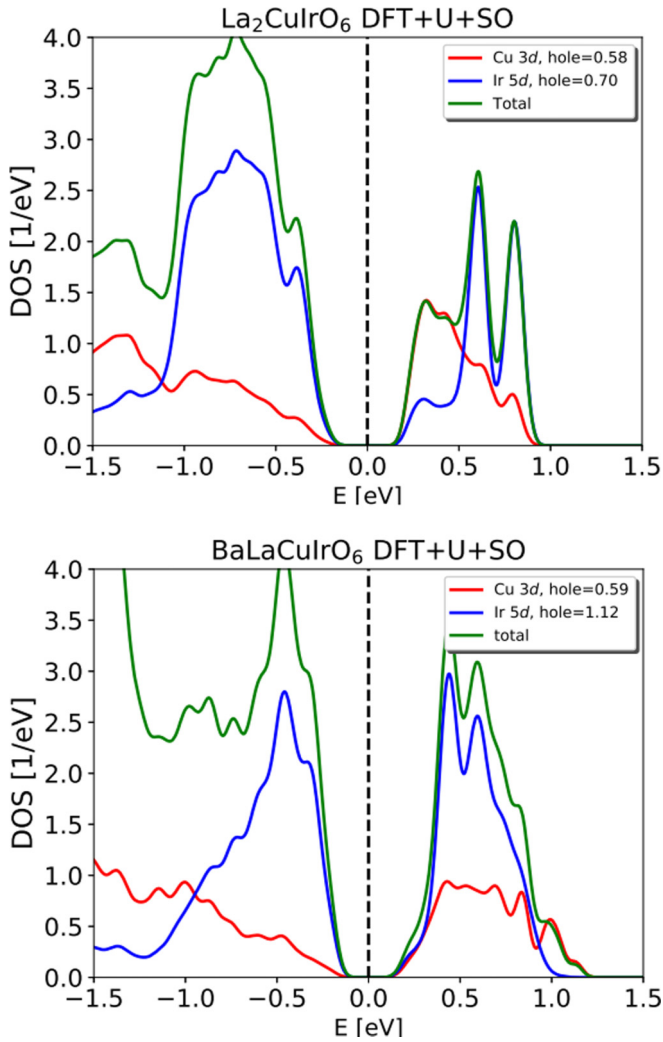


FIG. 9. DOS calculations of $\text{La}_2\text{CuIrO}_6$ and BaLaCuIrO_6 with SO (DFT+ U +SO). Both the U and SO values contribute to the insulating state of both compounds.

transfer transport [42]. This explanation is not satisfactory for $(\text{Ca}, \text{Ba})_x\text{La}_{2-x}\text{CuIrO}_6$ as no transitionlike change in the Seebeck coefficient is observed in Fig. 11 for any composition. In both the high- T_c cuprate systems [43] and the copper-manganate perovskite systems [44], the sign change is also accompanied by a change in entropy transport mechanism from semiconductorlike for holes to metal-like for electrons. In addition, in both of these studies, the metallic side shows a much smaller value for S than the semiconducting side. In contrast, as already noted, $S(x)$ for $\text{Ba}_x\text{La}_{2-x}\text{CuIrO}_6$ is large on both sides of the zero crossing—there are no adjustable parameters in Fig. 12. We can estimate how the doping level changes with x by inverting the Heikes formula and in Fig. 13 we plot $\zeta = N_h/N_d = 1/(\exp(eS_{320}(x)/k_B) + 1)$ versus x . We see that ζ ranges from 0.12 to 0.93, suggesting that Ba-induced hole doping is effective over the entire range and that the density of hopping sites is approximately 1 per formula unit.

The smooth variation of S with x implies that the significant structural changes across the series have little effect on the disorder that controls N_d . This is demonstrated by

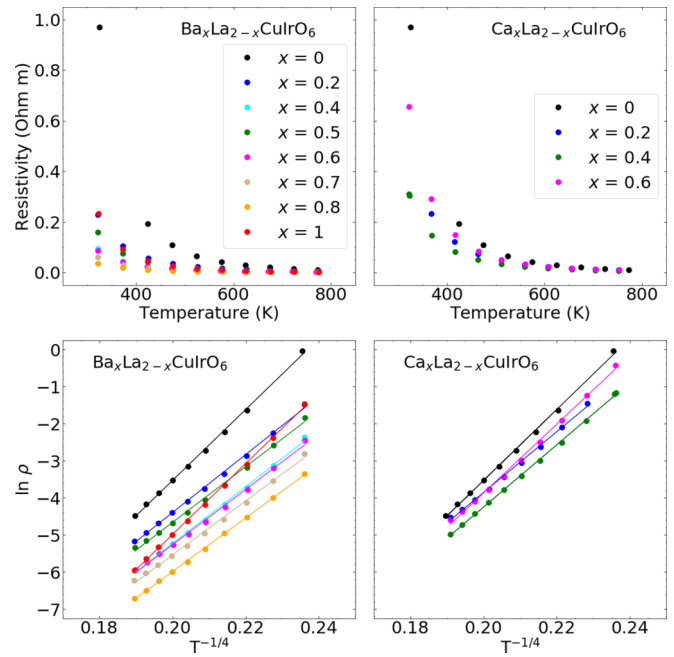


FIG. 10. Resistivity vs temperature (top) and variable-range charge hopping relationship plotted (bottom) for $\text{Ba}_x\text{La}_{2-x}\text{CuIrO}_6$ and $\text{Ca}_x\text{La}_{2-x}\text{CuIrO}_6$. The lines are linear fits to the VRH equation, $\ln(\rho) = (T_0/T)^{1/4} + \ln(\rho_0)$.

the comparison of thermopower behavior in $\text{Ba}_x\text{La}_{2-x}\text{CuIrO}_6$ and $\text{Ca}_x\text{La}_{2-x}\text{CuIrO}_6$. The much larger Ba^{2+} ion substituting into the La^{3+} increases the tolerance factor of the double perovskite structure to 0.995 which reduces the octahedral tilt. As a result, the Cu-O-Ir bond angles increase from an average of approximately 151° in $\text{La}_2\text{CuIrO}_6$ to 166° in BaLaCuIrO_6 , showing a clear reduction in tilting. This tilting transformation is not present in the Ca substitution; however a similar variation of S with x is observed. While we cannot rule out any change in N_d across the series, any such modulation would need to be compensated by a change in N_h that results in the nearly linear behavior in Fig. 13, which seems unlikely. Future work may involve performing measurements under pressure to ascertain the dependence of S with the carrier concentration fixed.

We believe this represents a way in which thermopower can be controlled for a nonmetallic system. This may be quite useful for thermoelectric materials discovery as both n - and p -type materials are needed for a fully functional thermoelectric device. Thermoelectric devices traditionally rely on doping of donor or acceptor states, such as in $(\text{Bi}, \text{Sb})_2(\text{Te}, \text{Se})_3$, to achieve both parts of the device [45]. Hole substitution via Ba^{2+} or Ca^{2+} in $\text{La}_2\text{CuIrO}_6$ produces both p - and n -type conduction and achieves a similar magnitude in thermopower. While $(\text{Ca}, \text{Ba})_x\text{La}_{2-x}\text{CuIrO}_6$ is too resistive to boast a good thermoelectric figure of merit, other double perovskites with lower resistivities should be explored for similar thermopower tuning.

E. Magnetic properties

The susceptibility for $\text{Ba}_x\text{La}_{2-x}\text{CuIrO}_6$ is shown in Fig. 14. The $\chi(T)$ data shown was obtained as the magnetization

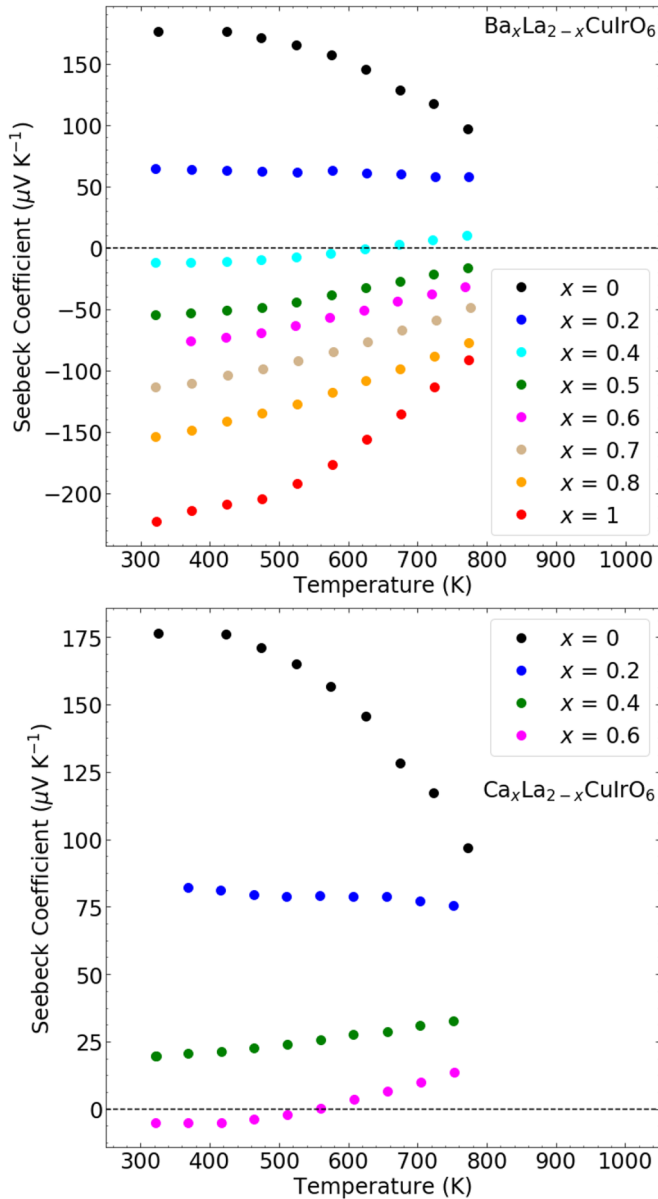


FIG. 11. Seebeck coefficient S vs temperature for $\text{Ba}_x\text{La}_{2-x}\text{CuIrO}_6$ (top) and $\text{Ca}_x\text{La}_{2-x}\text{CuIrO}_6$ (bottom). With increasing x , S decreases. This behavior is diminished as the temperature increases.

divided by field for $H = 0.1$ T. The data for $x = 0$ are consistent with those of Manna *et al.* [14], displaying temperature hysteretic behavior consistent with cluster-type spin glass freezing at a temperature $T_g = 71$ K. With increasing x , T_g decreases by about 10 K for $x = 1.0$. The inset of Fig. 14 shows zero field cooled (zfc) and field cooled (fc) data for $x = 0, 0.4, 0.6$, and 1.0 taken at 0.01 T. The lower field used for these measurements allows a more accurate determination of the frozen moment, χ_{frozen} , i.e., the difference in $\chi(2$ K) between fc and zfc data. Noting that the data are plotted on a logarithmic axis, one sees that χ_{frozen} is significantly larger for $x = 0$ than for the other x values.

The susceptibility for $\text{Ca}_x\text{La}_{2-x}\text{CuIrO}_6$ is shown in Fig. 15. The $\chi(T)$ data shown were obtained as the magnetization

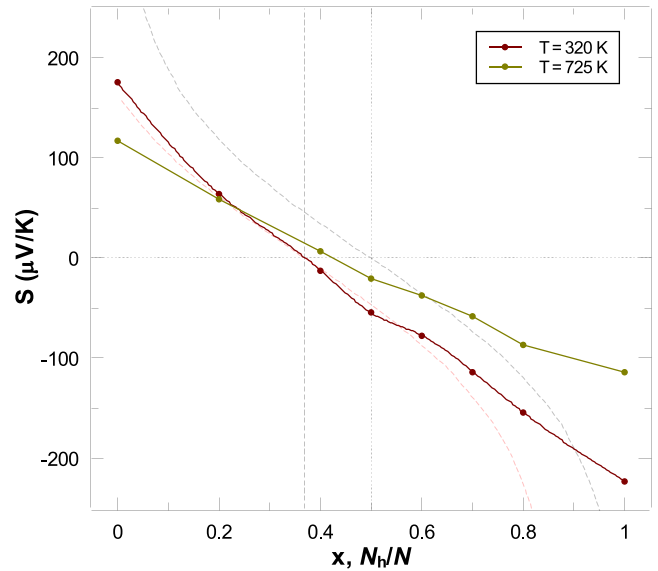


FIG. 12. Solid points are experimental values of S at 320 K and 725 K for $\text{Ba}_x\text{La}_{2-x}\text{CuIrO}_6$ vs x . The line connecting these points is a guide to the eye. The black dashed line is the Heikes formula for hole doping in a system with strongly correlated hopping. The red dashed line is the Heikes formula with the charge-neutrality point shifted to $x = 0.37$. The error bars for the data are smaller than the data symbols.

divided by field for $H = 0.1$ T. Here, the two data sets for each x below the peak correspond to zfc and fc protocols, indicating that the peak in $\chi(T)$ signals spin glass freezing. The reduction in T_g is less dramatic than seen for Ba substitution. In addition, contrary to the Ba-substitution case, the frozen moment actually increases with x after an initial decrease from the $x = 0$ data. This observed difference between data for $x = 0$ and $x = 0.1$ is much larger than seen for the Ba

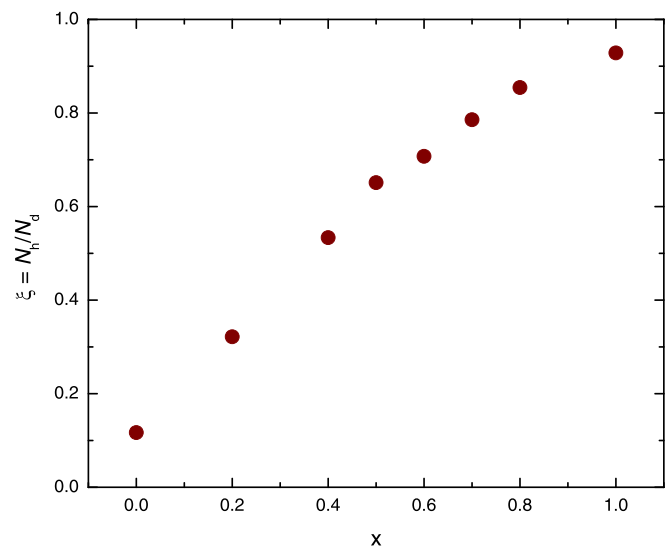


FIG. 13. The ratio of carrier density N_i to hopping site density N_d as a function of x , obtained from the Heikes formula, using the thermopower S at 320 K for $\text{Ba}_x\text{La}_{2-x}\text{CuIrO}_6$.

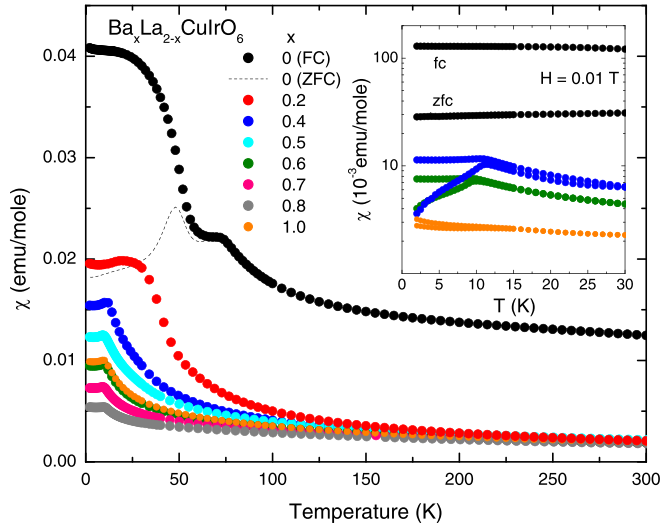


FIG. 14. The magnetic susceptibility at 0.1 T for $\text{Ba}_x\text{La}_{2-x}\text{CuIrO}_6$ is shown. The inset shows data collected at 0.01 T.

case between $x = 0$ and 0.2, a result that is consistent with the smaller size of Ca resulting in a more dramatic strain relief.

The magnetic susceptibility data shown in Figs. 14 and 15 show clear evidence for the type of temperature hysteresis commonly associated with the occurrence of spin glass freezing for $\text{Ba}_x\text{La}_{2-x}\text{CuIrO}_6$. For $\text{Ca}_x\text{La}_{2-x}\text{CuIrO}_6$ a similar hysteresis is observed, but at slightly higher temperatures, a nonhysteretic peak is observed at 60 K ($\text{Ca} = 0.2$) and 70 K ($\text{Ca} = 0.1$), which is likely due to the occurrence of AF ordering, consistent with the observations of Manna *et al.* [18].

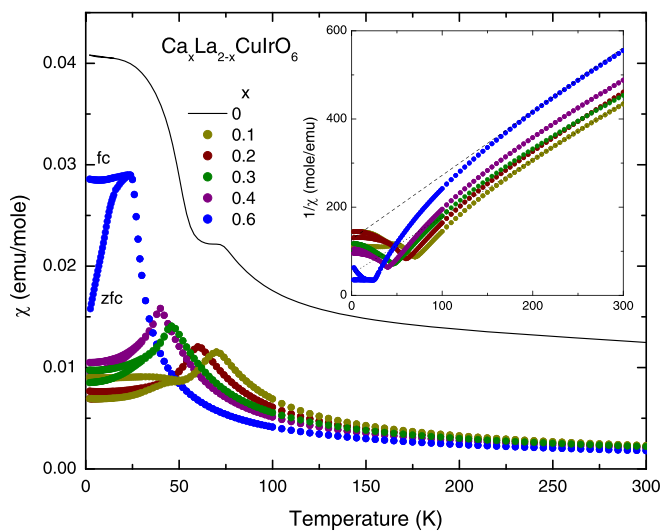


FIG. 15. The magnetic susceptibility at 0.1 T for $\text{Ca}_x\text{La}_{2-x}\text{CuIrO}_6$ is shown. The inset shows the inverse susceptibility which yields effective moment values of $2.49 \mu_B$ and $2.35 \mu_B$ for $x = 0.1$ and 0.6, respectively, as indicated by the dotted and dashed lines.

IV. CONCLUSION

The rock-salt ordered double perovskite, $\text{La}_2\text{CuIrO}_6$, was successfully substituted at the La site with Ba and Ca. A solid solution exists for $\text{Ba}_x\text{La}_{2-x}\text{CuIrO}_6$ with $0 \leq x \leq 0.8$ and 1 and for $\text{Ca}_x\text{La}_{2-x}\text{CuIrO}_6$ with $0 \leq x \leq 0.6$. Lattice parameters increase with increasing Ba content and decrease with increasing Ca content, consistent with the respective ionic radii of La^{3+} , Ba^{2+} , and Ca^{2+} [16]. Ba substitution also causes a change in symmetry from triclinic $P\bar{1}$ to monoclinic $P2_1/n$. XAS and RIXS measurements show primarily Ir is oxidizing to +4.7–4.8 in the BaLaCuIrO_6 solid-solution limit. The density of states calculated in DFT+ U +SO confirms the increase of the oxidation number of the Ir ion in BaLaCuIrO_6 and shows the importance of the SO effect on the gap opening at the Fermi energy via the enhanced electronic correlations.

Transport measurements reveal all compounds are insulating and follow the Heikes model for a three-dimensional variable range hopping semiconductor with strong onsite binding energies. The thermopower measurements show a change from p -type to n -type behavior, despite hole substitution. The variation of S with x in both Ca and Ba substitutions shows that the significant structural changes induced by Ba substitution do not significantly affect transport behavior. Rather transport is dominated by the carrier density, which increases with increasing x . The shift from p - to n -type conduction is consistent with the Heikes model in this scenario. Both Ba- and Ca-substituted compositions show spin-freezing behavior, with frozen moments decreasing with increasing substitutions, consistent with the reduction in spin state brought about by Ir^{4+} to Ir^{5+} oxidation.

This work presents an unusual mechanism whereby the thermopower can be reversed in an insulator. This kind of carrier sign control may be especially useful in situations where doping effectiveness of semiconductors is limited by other physiochemical interactions. Investigations of other double perovskites with requisite conductivities may yield interesting thermoelectric performance where both p - and n -type conduction are readily available.

ACKNOWLEDGMENTS

The work at Oregon State University (M.A.S.) was supported by the National Science Foundation Grant No. DMR-1508527. The magnetization measurements at UCSC (A.P.R.) were supported by the U.S. Department of Energy Office of Basic Energy Science, Division of Condensed Matter Physics under Award No. DE-SC0017862. Work at the Advanced Photon Source (D.H., J.K.) was supported by the U.S. Dept. of Energy Office of Science, Office of Basic Energy Sciences, under Award No. DE-AC02-06CH11357. DFT calculations (H.P.) were supported by the U.S. Department of Energy, Office of Science, Basic Energy Sciences, Materials Sciences and Engineering Division. H.P. gratefully acknowledges the computing resources provided on Bebop, a high-performance computing cluster operated by the Laboratory Computing Resource Center at Argonne National Laboratory.

- [1] R. Lindsay, W. Strange, B. L. Chamberland, and R. O. Moyer Jr., *Solid State Commun.* **86**, 759 (1993).
- [2] A. V. Powell and P. D. Battle, *J. Alloys Compd.* **191**, 313 (1993).
- [3] M. A. Subramanian, M. K. Crawford, R. L. Harlow, T. Ami, J. A. Fernandez-Baca, Z. R. Wang, and D. C. Johnston, *Physica C* **235-240**, 743 (1994).
- [4] M. Vogl, R. Morrow, A. A. Aczel, R. B. Rodriguez, A. U. B. Wolter, S. Wurmehl, S. Aswartham, and B. Büchner, *Phys. Rev. Materials* **4**, 054413 (2020).
- [5] K. Matsuhira, M. Wakeshima, Y. Hinatsu, and S. Takagi, *J. Phys. Soc. Jpn.* **80**, 094701 (2011).
- [6] M. Wakeshima, D. Harada, and Y. Hinatsu, *J. Alloys Compd.* **287**, 130 (1999).
- [7] P. D. Battle, G. R. Blake, T. C. Gibb, and J. F. Vente, *J. Solid State Chem.* **145**, 541 (1999).
- [8] P. D. Battle, J. G. Gore, R. C. Hollyman, and A. V. Powell, *J. Alloys Compd.* **218**, 110 (1995).
- [9] K. K. Wolff, L. H. Tjeng, and M. Jansen, *Solid State Commun.* **289**, 43 (2019).
- [10] B. Ranjbar, E. Reynolds, P. Kayser, and B. J. Kennedy, *Inorg. Chem.* **54**, 10468 (2015).
- [11] J. Flynn, J. Li, A. W. Sleight, A. P. Ramirez, and M. A. Subramanian, *Inorg. Chem.* **55**, 2748 (2016).
- [12] J. Flynn, J. Li, A. P. Ramirez, and M. A. Subramanian, *J. Solid State Chem.* **247**, 53 (2017).
- [13] A. V. Powell, J. G. Gore, and P. D. Battle, *J. Alloys Compd.* **201**, 73 (1993).
- [14] L. Bufaiçal, L. Mendonça. Ferreira, R. Lora-Serrano, O. Agüero, I. Torriani, E. Granado, P. G. Pagliuso, A. Caytuero, and E. Baggio-Saitovich, *J. Appl. Phys.* **103**, 07F716 (2008).
- [15] M. T. Haque, H. Satoh, and N. Kamegashira, *J. Alloys Compd.* **408-412**, 1205 (2006).
- [16] M. T. Haque, H. Satoh, and N. Kamegashira, *Mat. Res. Bull.* **39**, 2279 (2004).
- [17] S. Vasala and M. Karppinen, *Prog. Solid State Chem.* **43**, 1 (2015).
- [18] K. Manna, R. Sarkar, S. Fuchs, Y. A. Onyikienko, A. K. Bera, G. A. Cansever, S. Kamusella, A. Maljuk, C. G. F. Blum, L. T. Corredor, A. U. B. Wolter, S. M. Yusuf, M. Frontzek, L. Keller, M. Iakovleva, E. Vavilova, H. J. Grafe, V. Kataev, H. H. Klauss, D. S. Inosov, S. Wurmehl, and B. Buchner, *Phys. Rev. B* **94**, 144437 (2016).
- [19] X. Zhang, B. Li, J. Cheng, X. Chen, L. Wang, Z. Miu, Z. Song, F. Chi, S. Liu, and Z. H. Wang, *J. Phys.: Condens. Matter* **31**, 435601 (2019).
- [20] R. Shannon, *Acta Crystallogr.* **A32**, 751 (1976).
- [21] W. K. Zhu, J.-C. Tung, W. Tong, L. Ling, M. Starr, J. M. Wang, W. C. Yang, Y. Losovyj, H. D. Zhou, Y. Q. Wang, P.-H. Lee, Y.-K. Wang, Chi-Ken Lu, and S. X. Zhang, [arXiv:1608.07763](https://arxiv.org/abs/1608.07763).
- [22] H. Rietveld, *J. Appl. Crystallogr.* **2**, 65 (1969).
- [23] T. Gog, D. M. Casa, A. H. Said, M. H. Upton, J. Kim, I. Kuzmenko, X. Huang, and R. Khachatryan, *J. Synchrotron Radiat.* **20**, 74 (2013).
- [24] Yu. V. Shvyd'ko, J. P. Hill, C. A. Burns, D. S. Coburn, B. Brajuskovic, D. Casa, K. Goetze, T. Gog, R. Khachatryan, J.-H. Kim, C. N. Koditwakkku, M. Ramanathan, T. Roberts, A. Said, H. Sinn, D. Shu, S. Stoupin, M. Upton, M. Wiczorek, and H. Yavas, *J. Electron Spectrosc. Relat. Phenom.* **188**, 140 (2013).
- [25] G. Kresse and J. Furthmüller, *Phys. Rev. B* **54**, 11169 (1996).
- [26] G. Kresse and D. Joubert, *Phys. Rev. B* **59**, 1758 (1999).
- [27] J. P. Perdew, K. Burke, and M. Ernzerhof, *Phys. Rev. Lett.* **77**, 3865 (1996).
- [28] See Supplemental Material at <http://link.aps.org/supplemental/10.1103/PhysRevMaterials.5.054604> for more information about XRD patterns, unit cell angles, and DOS calculations.
- [29] V. M. Goldschmidt, *Die Gesetze der Krystallochemie. Naturwissenschaften* **14**, 477 (1926).
- [30] W. H. Baur, *Acta Crystallogr. Sect. B* **30**, 1216 (1974).
- [31] K. Robinson, G. V. Gibbs, and P. H. Ribbe, *Science* **172**, 567 (1971).
- [32] D. Altermatt and I. D. Brown, *Acta Crystallogr. Sect. B* **B41**, 240 (1985).
- [33] M. Kusch, V. M. Katukuri, N. A. Bogdanov, B. Buchner, T. Dey, D. V. Efremov, J. E. Hamann-Borrero, B. H. Kim, M. Krisch, A. Maljuk, M. M. Sala, S. Wurmehl, G. Aslan-Cansever, M. Sturza, L. Hozoi, J. van den Brink, and J. Geck, *Phys. Rev. B* **97**, 064421 (2018).
- [34] A. Nag, S. Bhowal, A. Chakraborty, M. M. Sala, A. Efimenko, F. Bert, P. K. Biswas, A. D. Hillier, M. Itoh, S. D. Kaushik, V. Siruguri, C. Meneghini, I. Dasgupta, and S. Ray, *Phys. Rev. B* **98**, 014431 (2018).
- [35] X. Liu, V. M. Katukuri, L. Hozoi, W.-G. Yin, M. P. M. Dean, M. H. Upton, J. Kim, D. Casa, A. Said, T. Gog, T. F. Qi, G. Cao, A. M. Tselvik, J. van den Brink, and J. P. Hill, *Phys. Rev. Lett.* **109**, 157401 (2012).
- [36] F. Nilsson, K. Karlsson, and F. Aryasetiawan, *Phys. Rev. B* **99**, 075135 (2019).
- [37] M. T. Czyżyk and G. A. Sawatzky, *Phys. Rev. B* **49**, 14211 (1994).
- [38] C. Bhandari, Z. S. Popović, and S. Satpathy, *New J. Phys.* **21**, 013036 (2019).
- [39] B. I. Shklovskii and A. L. Efros, *Electronic Properties of Doped Semiconductors* (Springer-Verlag, Berlin, 1984), p. 205.
- [40] P. M. Chaikin and G. Beni, *Phys. Rev. B* **13**, 647 (1976).
- [41] A. Maignan, D. Flahaut, and S. Hébert, *Eur. Phys. J. B* **39**, 145 (2004).
- [42] J. S. Zhou and J. B. Goodenough, *Phys. Rev. B* **60**, R15002 (1999).
- [43] S. D. Obertelli, J. R. Cooper, and J. L. Tallon, *Phys. Rev. B* **46**, 14928 (1992).
- [44] W. Kobayashi, I. Terasaki, M. Masashi, and R. Funahashi, *J. Phys. Soc. Jpn.* **73**, 523 (2004).
- [45] T. M. Tritt and M. A. Subramanian, *MRS Bull.* **31**, 188 (2006).